Impact of First-Principles Properties of Deuterium–Tritium on Inertial Confinement Fusion Target Designs

Introduction

Inertial confinement fusion (ICF) has been actively pursued in laboratories since the concept[1] was invented in 1972. In the conventional "hot-spot" ignition scheme, ICF capsules, consisting of a solid deuterium–tritium (DT) layer covered by an ablator, are driven to implode either by x rays in a hohlraum[2–4] or directly by lasers.[5,6] If properly designed, ICF targets can be compressed by shock waves and the spherical convergence to form an extremely dense (>1000× solid density) shell surrounding a high-temperature core (hot spot). A properly assembled core with an extremely high pressure (>100 ~ 300 Gbar) makes it possible not only to produce sufficient α particles from DT fusions but also to "bootstrap" the heat (α-particle stopping) in the hot spot.[7] If this occurs, a fusion burn wave could quickly propagate through the dense shell[8] and a net energy gain would be expected.

Designing and understanding ICF experiments rely on radiation–hydrodynamics simulations,[9–12] in which an accurate knowledge of properties of relevant materials (both DT fuel and ablators) under high-energy-density (HED) conditions is a prerequisite. To be specific, the equation of state (EOS) is needed to close the hydrodynamic equations.[13] The compressibility of material is determined by its EOS.[14] Besides the static EOS, an accurate knowledge of transport properties, such as thermal conductivity and viscosity, is also necessary for understanding the heat transport[15–17] and energy dissipation. In addition, the opacity of imploding capsules determines the radiation energy transport, which is also important in ICF simulations. Finally, the α-particle stopping power[18–20] of DT plasmas is also a prerequisite for ICF ignition simulations. The accuracy of these properties can affect the reliability of ICF target designs given that the margin for ignition to occur is usually quite small.

Studies of ICF ignition target designs[21–24] have revealed that the minimum laser energy scales as $E_L \propto \alpha^{1.9}$, with the adiabat α conventionally defined as the ratio of plasma pressure to the Fermi-degenerate pressure. This implies that to reduce the laser energy required for ignition, the imploding DT shell should be kept in a lower adiabat. Namely, maintaining a relatively lower temperature ($T \simeq 0.1$ to $0.2 \times T_F$, where T_F is the Fermi temperature) in the imploding DT capsule is key to obtaining higher compression and a larger energy gain for particular laser energy. As an example, the typical "path" of an imploding DT capsule on the temperature and density plane for a low-adiabat implosion (α = 1.5 to 3) is shown in Fig. 141.23. The in-flight DT shell in a low-adiabat implosion travels through a plasma region denoted as "warm dense matter" (WDM). Typically, the WDM regime for DT spans a density range from ρ = 1 to 200 g/cm^3 and temperatures of T = 1 to 200 eV, in which strong coupling and electron degeneracy are expected to be important. Warm dense plasmas are generally characterized by the Coulomb coupling parameter $\Gamma = q^2/(4\pi\epsilon_0 r_s k_B T)$ and the electron degeneracy parameter $\theta = T/T_F$, with the charge q, the Boltzmann constant k_B, and the interparticle distance $r_s = (3/4\,\pi n)^{1/3}$ for the particle density n. For WDM, $\Gamma \geq 1$ and $\theta \leq 1$. Even for the simplest element of hydrogen, accurate calculations of its properties in the WDM regime have been challenging in the past.

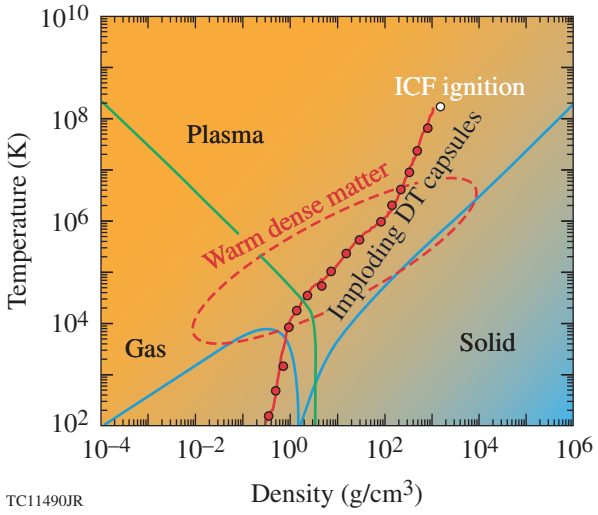

Figure 141.23
The density and temperature "path" of a low-adiabat imploding DT capsule to ICF ignition.

The many-body and quantum nature in such a complex system presents difficulties in handling WDM plasmas. Historically, approximate models were used to estimate the plasma properties in the WDM regime. For example, the extensively used *SESAME* EOS library[25] of DT and its updated version known as "*Kerley03*"[26] that is based on the chemical model of matter.[27] Although they have gained wide acceptance for a wide range of EOS parameters, such models may not be accurate enough to simulate WDM plasmas, especially for the old *SESAME* EOS that was widely used in hydrocodes. The thermal conductivity models, including the Lee–More model[28] and the *PURGATORIO* package,[29] are also extensively used in ICF simulations. These thermal conductivity models are based either on the first-order approximation to the Boltzmann equation or an average-atom scheme. They do not account fully for the many-body coupling and degeneracy effects in the WDM regime. Another example is the opacity of warm dense plasmas. The traditional astrophysics opacity table (AOT)[30] as well as the OPAL opacity project,[31] both of which were built for astrophysics applications, do not provide data in the WDM regime. Historically, the cold opacity of materials was patched for the WDM plasma condition in hydro simulations. Therefore, it is natural to ask how these approximated models may affect ICF simulations of low-adiabat implosions.

Taking advantage of the recent developments in first-principles (FP) methods, many studies on the properties of warm dense plasmas have been performed for both ICF applications and HED experiments in general. For instance, the EOS of deuterium/hydrogen has been investigated extensively using the path-integral Monte Carlo (PIMC) method,[32–37] the quantum-molecular dynamics (QMD) simulations,[38–49] and the coupled electron–ion Monte Carlo method.[50] These state-of-art calculations provided benchmarks for experimental measurements of the shock Hugoniot of hydrogen and deuterium.[51–58] In addition to the focus on the static EOS, the transport properties of warm dense hydrogen and its isotopes have also been revisited in recent years by FP simulations, especially the thermal/electric conductivities[59–65] and the viscosity.[64,66,67] Significant differences (by a factor of 3 to 10) in the WDM regime have been revealed between these models and the FP calculations of the thermal conductivity. In turn, these FP results have been used to improve the physics models[68] implemented in ICF hydrocodes. In addition, the electron–ion thermal equilibration has also been re-examined for ICF-relevant plasma conditions in recent years.[69–75] Most recently, the opacity of warm dense deuterium has been systematically investigated by QMD calculations[76] for the full range of ρ/T conditions covering the ICF implosion path. Again, orders-of-magnitude differences were identified when compared to the cold opacity that was patched to the AOT for ICF simulations. These FP calculations have been benchmarked with available experimental data of the principal Hugoniot and its optical reflectivity measurements.[77,78]

Besides the extensive studies of DT fuel, the FP methods have been applied to investigate the properties of ICF ablator materials such as plastic polystyrene (CH),[79–82] polyethylene,[83] beryllium and its mixture with CH,[63] as well as carbon.[84,85] The goal is either to systematically build complete tables of material properties under HED conditions or to perform FP calculations for a certain range of densities and temperatures to guide model improvements. Most importantly, these FP calculations can provide self-consistent properties of warm dense plasmas, while the self-consistency was often missing among the physics models adopted for ICF simulations. On the experimental side, ICF and HED experiments[86,87] equipped with accurate diagnostic tools such as x-ray Thomson scattering[88,89] have begun to provide detailed tests of various theoretical calculations.

Combining the FP methods of PIMC and QMD, we have systematically investigated the properties of deuterium over a wide range of densities and temperatures that fully cover the ICF implosion path. By mass scaling, the properties of DT can be derived from the deuterium properties. In previous publications, we have established the FP equation-of-state (FPEOS) table,[36,37] the thermal conductivity (κ_{QMD}),[65] and the FP opacity table (FPOT)[76] of the DT fuel for ICF applications. In this article we focus on their combined effects on the hydro predictions of ICF target designs by comparing them with the traditional model simulations. We found that the one-dimensional (1-D) predictions of ICF implosions, by comparing the FP-based properties of DT and traditional models, can change by up to a factor of ~2.5 in terms of neutron yield and energy gain; the lower the adiabat o f an imploding DT capsule, the more deviations expected. A reliable design of ICF ignition targets demands the use of the FP-based properties of DT.

This article is organized as follows: The next two sections (1) describe the two FP methods of PIMC and QMD and (2) the first-principles–based EOS, thermal conductivity, and opacity of warm dense deuterium compared with available experiments, other *ab initio* calculations, and the traditional model predictions. The significant discrepancies are also illustrated among these comparisons. The combined effects of these FP-based properties to ICF target designs are then presented by hydro-simulation comparisons of ICF implosions on both the OMEGA laser and the National Ignition Facility (NIF).

Finally, these results are summarized and future FP studies on ICF-relevant ablator materials are briefly mentioned.

The First-Principles Methods of PIMC and QMD for Warm Dense Plasmas

Understanding the properties of warm dense plasmas is challenging because of the many-body coupling and quantum degeneracy effects intrinsic to such complicated systems. It demands the full treatment of both effects using the fundamental principles governing a quantum many-body system. Among the various FP methods, PIMC and QMD have been extensively applied for studies of warm dense plasmas. Each of the two FP methods is briefly described in the following subsections.

1. Path-Integral Monte Carlo

A many-body quantum system in thermodynamic equilibrium can be described by the density matrix

$$\rho(\mathbf{R},\mathbf{R}';\beta)=\sum_n \phi_n(\mathbf{R})\phi_n(\mathbf{R}')e^{-E_n/k_\mathrm{B}T},$$

with $\beta = 1/k_\mathrm{B}T$, ϕ_n the eigenstates, and E_n the eigenenergy of the system. The eigenstates of an interacting quantum system are unknown, however, and no efficient numerical method exists to indirectly compute the density matrix. The fundamental idea of the path-integral approach is based on the convolution property of $\rho(\mathbf{R},\mathbf{R}';\beta)$. Namely, the density matrix at temperature T can be expressed as a convolution of density matrices at an M times higher temperature, $M \times T$:

$$\rho(\mathbf{R},\mathbf{R}';\beta)=\int \mathrm{d}\mathbf{R}_1\mathrm{d}\mathbf{R}_2\ldots\mathrm{d}\mathbf{R}_{M-1}\rho(\mathbf{R},\mathbf{R}_1;\Delta\beta)$$
$$\times\rho(\mathbf{R}_1,\mathbf{R}_2;\Delta\beta)\cdots\rho(\mathbf{R}_{M-1},\mathbf{R}';\Delta\beta). \quad (1)$$

At a high temperature, the correlation effects betwee n particles are small and a very good approximation for the density matrix exists.[90] The path integral is needed to recover the full correlation effects at a lower temperature. The integral on the right-hand side of Eq. (1) can be interpreted as a weighted average over all *paths* that connect the points $\mathbf{R}$ and $\mathbf{R}'$. $\mathbf{R}$ is a collective variable that denotes the positions of all particles $\mathbf{R} = \{\mathbf{r}_1,\ldots\mathbf{r}_N\}$. β represents the length of the path in "imaginary time," and $\Delta\beta = \beta/M$ is the size of each of the M time steps. In PIMC calculations, electrons and ions are treated on equal footing as paths, which means the quantum effects of both species are included consistently, although for the temperatures under consideration, the zero-point motion and exchange effects of the nuclei are negligible.

One can consequently interpret the positions $\mathbf{R}_1\ldots\mathbf{R}_{M-1}$ as intermediate points on a path from $\mathbf{R}$ and $\mathbf{R}'$. The multidimensional integration over all paths in Eq. (1) can be carried out efficiently by the Monte Carlo method.[91] Observables associated with an operator $\hat{O}$ can be derived from

$$\langle\hat{O}\rangle=\frac{\int \mathrm{d}\mathbf{R}\int \mathrm{d}\mathbf{R}'\langle\mathbf{R}|\,\hat{O}\,|\mathbf{R}'\rangle\rho(\mathbf{R}',\mathbf{R};\beta)}{\int \mathrm{d}\mathbf{R}\rho(\mathbf{R}',\mathbf{R};\beta)}. \quad (2)$$

For the kinetic and potential energies, E_K and E_P, as well as for pair correlation functions, only diagonal matrix elements $(\mathbf{R}' = \mathbf{R})$ are needed.

Since electrons are fermions, their fermionic character matters for the degenerate plasma conditions under consideration. This implies that one must construct an antisymmetric many-body density matrix, which can be derived by introducing a sum of all permutations $\mathcal{P}$ and then also include paths from $\mathbf{R}$ to $\mathcal{P}\mathbf{R}'$. While this approach works well for bosons,[91] for fermions each permutation must be weighted by a factor $(-1)^{\mathcal{P}}$. The partial cancellation of contributions with opposite signs leads to an inefficient algorithm when the combined position and permutation space are sampled directly.[91] This is known as the *Fermion sign problem*, and its severity increases as the plasma temperature decreases (becoming more degenerate). In our PIMC calculations, we deal with the Fermion sign problem by using the free-particle nodes,[92] although the nodes of a variational density matrix[93] have also been employed in other PIMC computations.[94,95] The details of our PIMC simulations of warm dense deuterium can be found in previous publications.[36,37]

In PIMC simulations, we approach the low-T density matrix from the known high-T ones through multidimensional integrations along the "temperature path." As the plasma temperatures decrease, the Fermi-sign problem prevents the efficient evaluation of the multidimensional integrations in the combined position and permutation space. Therefore, the lowest temperatures in our restricted PIMC calculations have only reached $T \simeq 0.1$ to $0.2 \times T_\mathrm{F}$. For even lower plasma temperatures, other FP methods should be used. The QMD method is one of the FP methods that can handle low-T plasmas.

2. Quantum-Molecular Dynamics

The QMD method is based on the finite-temperature density functional theory.[96–98] The many-electron system in a plasma can be described by a wave function $\Psi(\mathbf{r}_1,\mathbf{r}_2,\ldots\mathbf{r}_N)$, which satisfies the following Schrödinger equation (atomic units used throughout):

$$\left[-\frac{1}{2}\sum_i \Delta_i + \sum_i V(\mathbf{r}_i) + \sum_{i\neq j}\frac{1}{|\mathbf{r}_i-\mathbf{r}_j|}\right]\Psi = E\Psi. \quad (3)$$

The second term in Eq. (3) is the electron–ion interaction, while the third term describes the Coulomb repulsion among electrons. To solve the above Schrödinger equation, a tractable way is to map the many-electron wave function onto a one-electron basis, $\Psi(\mathbf{r}_1\mathbf{r}_2,\ldots,\mathbf{r}_N)\rightarrow\{\psi(\mathbf{r}_1),\psi(\mathbf{r}_2),\ldots,\psi_N(\mathbf{r}_N)\}$. The Kohn–Sham density functional theory[96,97] (DFT) is an efficient "mean-field" theory for many-electron systems, in which the total wave function takes a product form of individual one-electron "orbital," $\Psi_i(\mathbf{r})$. By doing so, Eq. (3) can be casted into the well-known Kohn–Sham equation for the orbital $\Psi_i(\mathbf{r})$:

$$\left\{-\frac{1}{2}\Delta + V_z(\mathbf{r}) + V_{\mathrm{H}}[\rho](\mathbf{r}) + V_{xc}[\rho](\mathbf{r})\right\}\psi_i(\mathbf{r}) = E_i\psi_i(\mathbf{r}), \quad (4)$$

with the electron density and the Hartree term defined as

$$\rho(\mathbf{r}) = \sum_{i=1}^{N}|\psi_i(\mathbf{r})|^2; \quad V_{\mathrm{H}}[\rho](\mathbf{r}) = \int\frac{\rho(\mathbf{r}')}{|\mathbf{r}-\mathbf{r}'|}\mathrm{d}\mathbf{r}'. \quad (5)$$

Since the exchange-correlation term V_{xc} and the Hartree term depend on the electron density $\rho(\mathbf{r})$, which is again a function of $\psi(\mathbf{r})$, the Kohn–Sham equation can be solved in a self-consistent way. Together with the ionic force, the resulting electronic force is then used to drive the classical ionic motion through Newton's equation under the Born–Oppenheimer approximation (in a QMD step).

Our QMD simulations have been performed within the Mermin's finite-temperature DFT,[98] which was implemented in the Vienna *ab initio* simulation package (VASP)[99,100] using a plane-wave basis. The generalized gradient approximation (GGA) with the Perdew–Burke–Ernzerhof (PBE) exchange-correlation function[101] is employed in our QMD simulations. The electron–ion interaction is modeled by either the projector augmented wave (PAW) pseudopotentials or the pure Coulomb potential. The system was assumed to be in local thermodynamic equilibrium with equal electron and ion temperatures ($T_{\mathrm{e}} = T_{\mathrm{i}}$). The isothermal ensemble was used for our QMD simulations in which the number of particles, volume, and temperature was kept constant. For periodic boundary conditions, the electron wave function can be described by Bloch waves, consisting of products of plane waves with different momenta $\hbar k$ and a periodic function of space. Each k point in the first Brillouin zone uniquely defines every Bloch state. For each QMD step, a set of electronic wave functions for each k point is self-consistently determined for a given ionic configuration. Then, the ions are moved classically with a velocity Verlet algorithm, according to the combined ionic and electronic forces. The ion temperature was kept constant through simple velocity scaling. Repeating these QMD steps, a set of self-consistent ion trajectories and electronic wave functions can be found. These trajectories provide a self-consistent set of static, dynamic, and optical properties of warm dense plasmas. The details of our QMD simulations of warm dense deuterium plasmas can be found in recent publications.[65,76]

3. Calculating Plasma Properties from PIMC and QMD Simulations

For PIMC simulations, only the EOS was derived. The total internal energy follows from $E = E_{\mathrm{K}} + E_{\mathrm{P}}$, where E_{K} and E_{P} are the kinetic and potential energies, respectively. The pressure P can be obtained from the virial theorem for Coulomb systems, $P = (2E_{\mathrm{K}} + E_{\mathrm{P}})/3V$ with the volume V. The tabulated FPEOS of deuterium from PIMC calculations can be found in Ref. 37. In QMD simulations, the EOS of warm dense deuterium was calculated in a straightforward fashion by evaluating the electron term, then adding the contribution from the classical ions. Using QMD simulations, we have extended the PIMC-derived FPEOS table from the PIMC's lowest temperature of $T = 15{,}625$ K down to a much lower temperature of $T = 1000$ K for most of the density points ($\rho_D \geq 0.1$ g/cm^3). Dynamical and optical properties are determined from the QMD trajectories by calculating the velocity dipole matrix elements. Namely, from the resulting QMD trajectories, we choose uncorrelated snapshots of these configurations to calculate the velocity dipole matrix elements D_{mn} using the wave functions. The quantity D_{mn} is then applied to compute the frequency-dependent Onsager coefficients within the Kubo–Greenwood formalism:[102]

$$L_{ij}(\omega) = \frac{2\pi(-e)^{4-i-j}}{3Vm_{\mathrm{e}}^2\omega}\sum_{mn}F_{mn}|D_{mn}|^2 \times\left(\frac{E_m+E_n}{2}-H\right)^{i+j-2}\delta(E_m-E_n-\hbar\omega), \quad (6)$$

where $V = 1/\rho$ is the atomic volume, $E_m(E_n)$ is the energy of the mth (nth) state, and H is the enthalpy per atom of the system. The quantity of F_{mn} is the difference between the Fermi–Dirac distributions for states m and n at temperature T. The Onsager coefficients essentially determine the transport and optical properties of the system.

To calculate the electron thermal conductivity of a plasma, the linear response of the plasma to an electric field **E** and a temperature gradient ∇T is considered. The resulting electric current $\mathbf{j}_e$ and the heat flux $\mathbf{j}_q$ can be expressed as

$$\mathbf{j}_e = \left(eL_{11}\mathbf{E} - \frac{L_{12}\nabla T}{T}\right)\Big/ e, \tag{7}$$

$$\mathbf{j}_q = \left(eL_{21}\mathbf{E} - \frac{L_{22}\nabla T}{T}\right)\Big/ e\,. \tag{8}$$

For plasmas having no electric current ($\mathbf{j}_e = 0$), the above equations in combination with the definition of $j_q = -\kappa\nabla T$ give the thermal conductivity (in atomic units of $\hbar = m_e = e = 1$):

$$\kappa = \frac{L_{22} - L_{12}^2 \big/ L_{11}}{T} \tag{9}$$

with the Onsager coefficients given by L_{ij} in Eq. (6). If there is no temperature gradient ($\nabla T = 0$), Eq. (7) reduces to the Ohm's law with the real electrical conductivity of $\sigma_1 = L_{11}$.

The opacity calculations rely on the evaluation of the frequency-dependent absorption coefficient $\alpha_K(\omega)$, which is related to the electrical conductivity and the index of refraction (n) of the plasma:

$$\alpha_K(\omega) = \frac{4\pi\sigma_1(\omega)}{cn(\omega)} \tag{10}$$

with the speed of light c. To calculate the refractive index n, we start from the real part of the electrical conductivity, $\sigma_1(\omega) = L_{11}(\omega)$, and determine the imaginary part from the principal value integral:

$$\sigma_2(\omega) = -\frac{2}{\pi}P\int \frac{\omega\sigma_1(\omega')}{\omega'^2 - \omega^2}\mathrm{d}\omega'. \tag{11}$$

The dielectric function $\epsilon(\omega) = \epsilon_1(\omega) + i\epsilon_2(\omega)$ can be calculated from the following expressions:

$$\epsilon_1(\omega) = 1 - \frac{4\pi}{\omega}\sigma_2(\omega),$$

$$\epsilon_2(\omega) = 1 - \frac{4\pi}{\omega}\sigma_1(\omega). \tag{12}$$

Using the dielectric function, we compute the real [$n(\omega)$] and imaginary [$k(\omega)$] parts of the refractive index:

$$n(\omega) = \sqrt{\frac{\left|\epsilon(\omega)\right| + \epsilon_1(\omega)}{2}},$$

$$k(\omega) = \sqrt{\frac{\left|\epsilon(\omega)\right| - \epsilon_1(\omega)}{2}}. \tag{13}$$

The frequency-dependent reflectivity is given by

$$R(\omega) = \frac{\left[n(\omega) - n_0\right]^2 + k(\omega)^2}{\left[n(\omega) + n_0\right]^2 + k(\omega)^2} \tag{14}$$

with the refraction index n_0 of the ambient environment ($n_0 = 1$ for vacuum). Finally, the mass absorption coefficient (α_m) is equal to the absorption coefficient (α_K) divided by the mass density:[103]

$$\alpha_m(\omega) = \frac{\alpha_K(\omega)}{\rho} = \frac{4\pi\bar{\sigma}_1(\omega)}{nc\bar{n}(\omega)} \times \frac{1}{\rho}. \tag{15}$$

The "bar" over σ_1 and n stands for averaging over the uncorrelated configuration snapshots being sampled. We found that five to ten snapshots generally give a good statistic with variation less than ~5%.

Under the multigroup diffusion approximation, the Rosseland (K_R) and Planck (K_P) mean opacities are used for the radiation transport and emission calculations in hydrodynamic simulations. The grouped Rosseland and Planck mean opacities are defined as

$$K_R(\omega_1{:}\omega_2) = \frac{\int_{\omega_1}^{\omega_2} n(\omega)^2 \dfrac{\partial B(\omega,T)}{\partial T}\mathrm{d}\omega}{\int_{\omega_1}^{\omega_2} n(\omega)^2 \dfrac{1}{\alpha_m}\dfrac{\partial B(\omega,T)}{\partial T}\mathrm{d}\omega}, \tag{16}$$

$$K_P(\omega_1{:}\omega_2) = \frac{\int_{\omega_1}^{\omega_2} n(\omega)^2 \alpha_m(\omega) B(\omega,T)\mathrm{d}\omega}{\int_{\omega_1}^{\omega_2} n(\omega)^2 B(\omega,T)\mathrm{d}\omega} \tag{17}$$

for a group of photon energies between $\hbar\omega_1$ and $\hbar\omega_2$. Here, the Planck function $B(\omega,T) = \left(\hbar\omega^3/4\pi^3c^2\right)/\left(e^{\hbar\omega/k_BT} - 1\right)$ depends on the emitting photon energy and the plasma temperature. Integrating the frequency from $\omega_1 = 0$ to $\omega_2 = \infty$, one obtains the total Rosseland and Planck mean opacities.

Comparisons of FP-Based Properties of Deuterium with Experiments and Models

With the PIMC and QMD methods, we have calculated the EOS, thermal conductivity κ, and opacity of deuterium for a wide range of densities and temperatures. From the combined PIMC/QMD calculations, the FPEOS table[36,37] covers the deuterium plasma conditions of $\rho = 0.002$ to 1596 g/cm^3 and $T = 0.086$ eV to 5.5 keV. While for QMD calculations of κ and opacity, we have considered the deuterium plasma ranges of $\rho = 0.1$ to 673.5 g/cm^3 and $T = 5000$ K up to the Fermi temperature T_F. These density and temperature points fully cover the typical shell conditions in low-adiabat ICF implosions. It is noted that DFT-based QMD and PIMC results have been combined in the past for the shock Hugoniot studies of hydrogen,[34] helium,[94,95] carbon,[84] and water.[81] In this section, we compare the FP-calculated properties of deuterium plasma with both model predictions and available experimental data.

In Fig. 141.24, our PIMC/QMD–predicted (a) pressure and (b) energy are plotted as a function of the plasma temperature for the case of $\rho_D \simeq 7.391$ g/cm^3. They are compared with a recent *ab initio* calculation,[48] using a different molecular-dynamics code (*ABINIT*[104]), which combines both the orbital-based and orbital-free density functional theories (QMD–OFMD). The solid red circles represent our QMD results, while the open blue squares represent the PIMC calculations and the open green diamonds are those given by Wang *et al.*[48] It is noted that all the internal energies shown are referenced to the ground-state energy ($E_0 = -15.886$ eV) of a D_2 molecule. Figure 141.24 shows that in the warm dense regime, where both PIMC and QMD are valid, the two calculations result in almost identical EOS values. The PIMC simulations, however, are applicable only to $T \sim 10$ eV for this density because as the plasma temperature decreases, the Fermi-sign problem in PIMC prevents the efficient evaluation of degeneracy effects. In the low-T regime ($T < 0.2 \times T_F$), the QMD results are complimentary to the PIMC results. Overall, our combined EOS results from PIMC/QMD simulations compare well with the values given by QMD–OFMD calculations.[48] As expected, Fig. 141.24(a) shows almost constant pressures at $T \ll T_F$. This is attributed to the dominant electron degeneracy pressure at plasma temperatures well below the Fermi temperature ($T_F \simeq 61.9$ eV for this density).

Figure 141.25 compares the FPEOS-predicted Hugoniot of deuterium with extensively used EOS models of *SESAME*[25] and the updated *Kerley03*,[26] as well as the laser-shock experiments by Hicks *et al.*[57] and by Boehly *et al.*;[105] the Z-machine data by Knudson *et al.*;[54,55] and that of Boriskov *et al.*[106] The pressure of shocked deuterium is plotted as a function of the compression (ρ/ρ_0). The Hugoniot temperatures are marked in Fig. 141.25(a). Figure 141.25(a) indicates that the FPEOS-predicted Hugoniot is softer than *SESAME* at $P < 2.5$ Mbar (1 Mbar = 100 GPa), while it is stiffer in the pressure range of $P = 2.5$ to 100 Mbar. The

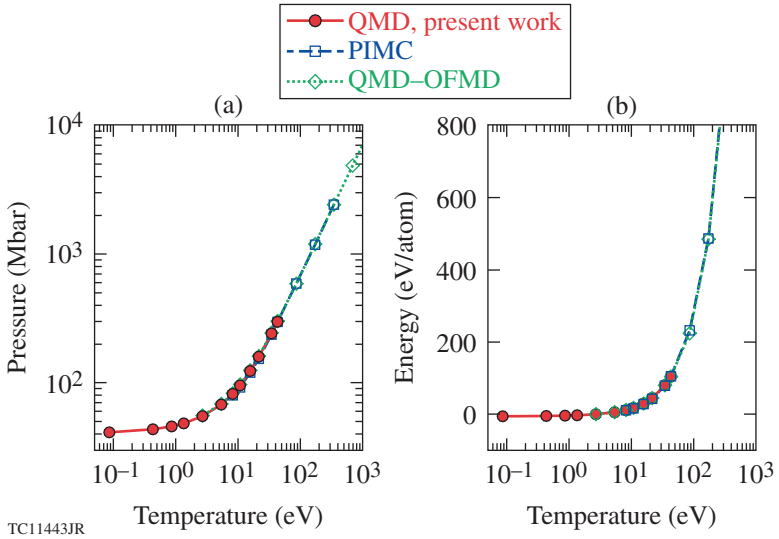

Figure 141.24
(a) The pressure and (b) energy as a function of temperature for $\rho_D = 7.391$ g/cm^3 are compared among different first-principles calculations: the current QMD calculations, the PIMC calculations,[37] and the QMD–OFMD calculations by Wang *et al.*[48]

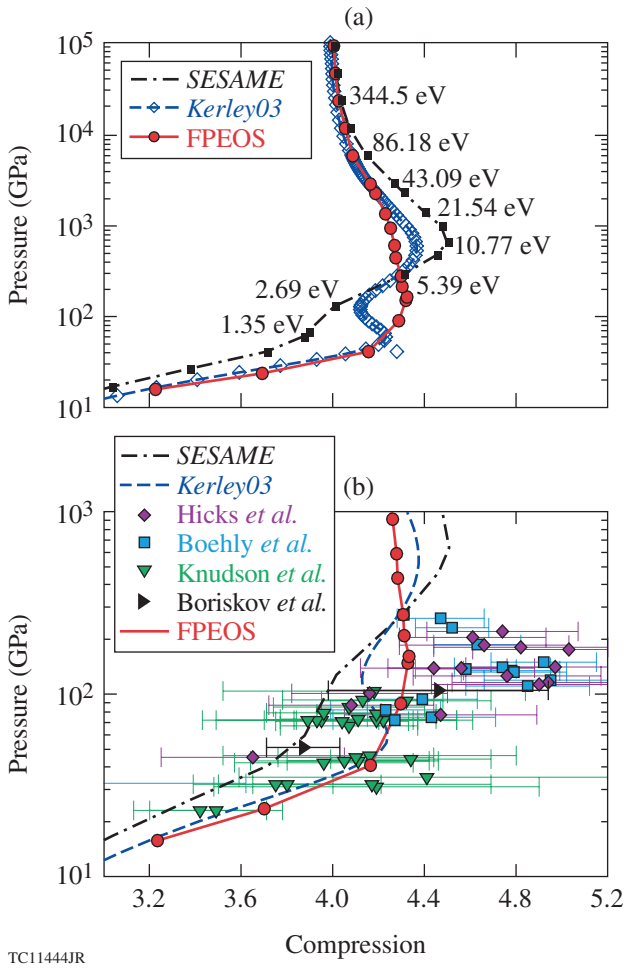

Figure 141.25
(a) The comparison of principal Hugoniot of deuterium among FPEOS, *SESAME*, and *Kerley03*; (b) their comparisons with available experimental data: the single-shock data published in Hicks *et al.*,[57] the OMEGA data derived from double-shock experiments by Boehly *et al.*,[105] the Z-machine data by Knudson *et al.*,[54,55] and the experiment by Boriskov *et al.*[106]

improved *Kerley03*, with including the molecular dissociation, quantum corrections, and a new ionization equilibrium model, gave Hugoniot values that were overall closer to the FPEOS. The slightly softer behavior is still seen, however, in *Kerley03* at pressures of $P \simeq 2.5$ to 10 Mbar, and the similar stiffer behavior at low pressure (P = 0.5 to 2 Mbar) is still less favorably compared with laser shock experiments than the FPEOS in this low-T range, as indicated by Fig. 141.25(b). The FPEOS Hugoniot is a bit closer to, but still not as soft as, what is indicated by the laser-shock experiments. To our best knowledge, this much-softer behavior[51,52,57,105] in these laser-shock experiments at $P \simeq 1$ to 2 Mbar has not yet been fully reproduced by *ab initio* calculations.

In Figs. 141.26 and 141.27, we compare the FPEOS with *SESAME*, *Kerley03*, and the classical Debye plasma model for a wide range of densities and temperatures. In these figures, we have normalized the pressure and energy of deuterium plasma by their *ideal* values, respectively. The *ideal* pressure (P_{id}) and energy (E_{id}) are the sum of contributions from the noninteracting Fermi electron gas together with classical ions. The deviations from these *ideal* values indicate the contribution from the Coulomb interactions. Figure 141.26 plots the normalized (a) pressure and (b) energy as a function of deuterium density for a plasma temperature of $T \simeq 10.77$ eV.

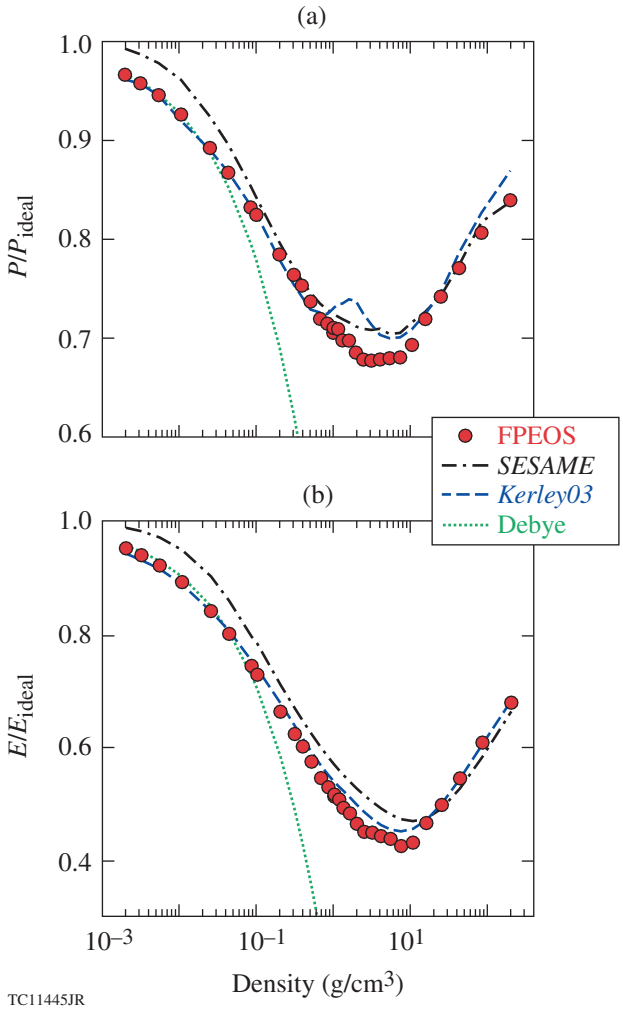

Figure 141.26
The normalized (a) pressure and (b) energy as a function of deuterium density for a plasma temperature at $T \simeq 10.77$ eV are compared among FPEOS, *SESAME*, *Kerley03*, and the classical Debye plasma model. The normalization is done with P_{id} and E_{id}, the total pressure and energy, respectively, for the ideal Fermi gas of electrons and the classical ions.

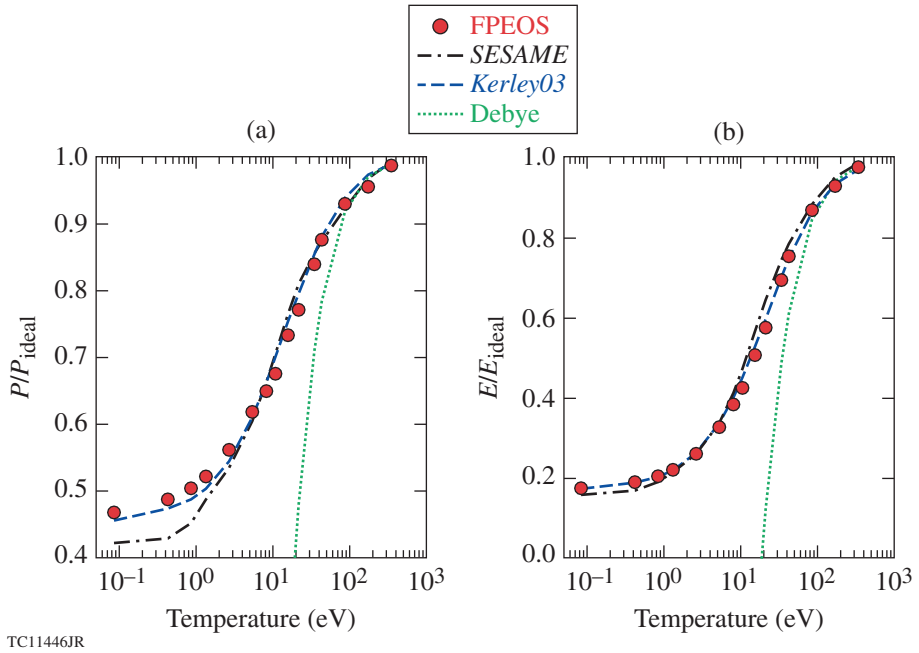

Figure 141.27
The normalized (a) pressure and (b) energy as a function of plasma temperature for the deuterium density of $\rho_D \simeq 7.391$ g/cm^3 are compared among FPEOS, *SESAME*, *Kerley03*, and the Debye model.

One sees that at very low densities the plasma is approaching a classical *ideal* gas; while as the density increases, both the pressure and energy decrease, which manifests the increasing Coulomb interactions among electrons and ions. Both reach a minimum at densities of several g/cm^3 for this temperature ($T \simeq 10.77$ eV), where the warm dense regime is located. As the density continues to increase, the Fermi degeneracy of electrons starts to become more dominant than electron–ion interactions so that the *ideal* Fermi gas is being approached. Namely, the ratios of both P/P_{id} and E/E_{id} gradually increase toward ~1 at high densities. As can be seen in Fig. 141.26, the *SESAME* model underestimates the electron–ion Coulomb interactions, even in the classical regime ($\rho_D < 0.1$ g/cm^3). The improved *Kerley03* and the classical Debye model better agree with the FPEOS in this low-density regime. The Debye model fails as plasma density increases to above 0.1 g/cm^3 because of its overestimated electron screening and the lack of electron degeneracy. In the warm dense regime of $\rho_D \simeq 1$ to 10 g/cm^3, both the *SESAME* and *Kerley03* models underestimated the Coulomb interactions between electrons and ions. In contrast to the FPEOS, both gave higher pressure and energy in this regime. The *Kerley03* model showed an unphysical pressure bump around $\rho_D = 1$ to 3 g/cm^3, which has also been noticed and modified in a recent EOS study at Livermore.[46] In Fig. 141.27, the normalized (a) pressure and (b) energy are plotted as a function of plasma temperature for the deuterium density of $\rho_D = 7.391$ g/cm^3. The *SESAME* model underestimates the pressure at low temperatures ($T < 1$ eV). As the plasma temperature increases to the high end, the system exhibits classical behavior as expected. In the warm dense regime ($T \simeq 10$ to 50 eV for this density), *SESAME* disagrees more with the FPEOS than the improved *Kerley03,* especially for the energies illustrated by Fig. 141.27(b).

For the transport and optical properties of warm dense deuterium, there were no direct measurements of thermal conductivity and opacity for the various densities and temperatures explored here. However, the optical reflectivity measurements[77,78] along the principal Hugoniot have been performed on both Nova and OMEGA, which enable us to make direct comparisons with our QMD calculations. In Figs. 141.28(a) and 141.28(b), the optical reflectivity versus the shock speed has been compared with both the recent OMEGA experiment[78] and an earlier Nova experiment[77] for different VISAR (velocity interferometer system for any reflector) wavelengths of $\lambda = 532$ nm and $\lambda = 808$ nm, respectively. The OMEGA experiments were taken from a decayed shock in deuterium for many shots. The experimental results are in good agreement with our QMD calculations. The early Nova experiment also compares well with other *ab initio* calculations.[41,43] This experimental confirmation lends credence to the L_{11} coefficients produced in our QMD studies of reflectivity and, in turn, to the other self-consistently calculated Onsager coefficients that determine thermal conductivity as well as the opacities.

Next, we compare the QMD-calculated κ with the Lee–More model prediction in Figs. 141.29(a) and 141.29(b) as a function of plasma temperature for densities of $\rho_D = 7.391$ g/cm^3 and

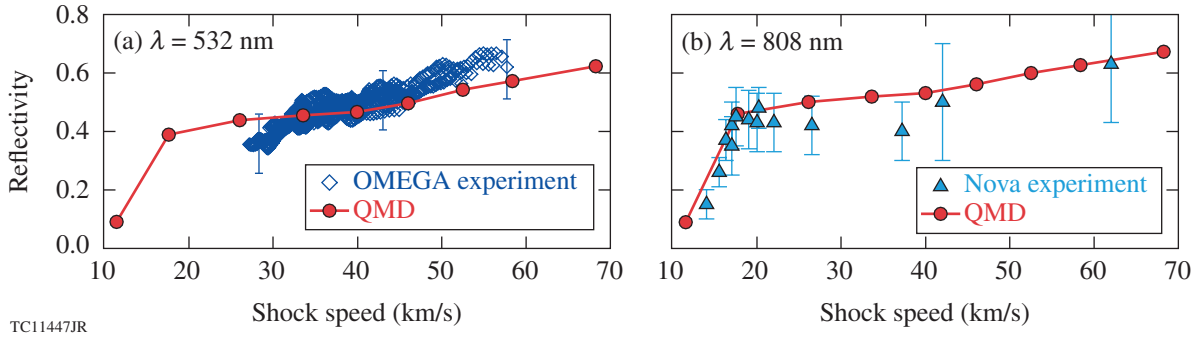

Figure 141.28
The comparison of reflectivity along the principal Hugoniot of deuterium between experiments and QMD calculations, for different VISAR wavelengths of (a) λ = 532 nm (OMEGA experiments) and (b) λ = 800 nm (Nova experiments).

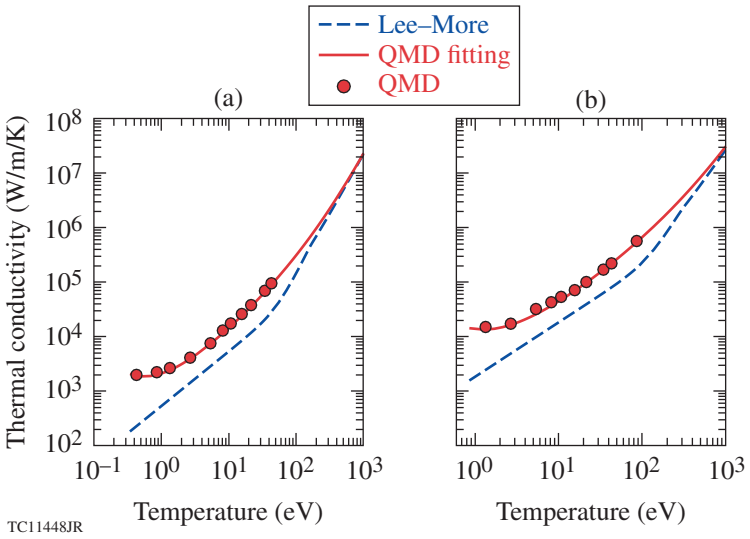

Figure 141.29
The QMD-predicted thermal conductivity κ of deuterium as a function of plasma temperature for densities of (a) $\rho_D \simeq 7.391$ g/cm^3 and (b) $\rho_D \simeq 24.945$ g/cm^3, which are compared with the Lee–More model and the fitting formula of Eqs. (19) and (20).

ρ_D = 24.945 g/cm^3, respectively. For each density point, the κ_{QMD} calculations have been performed to the highest temperature, approaching $T \simeq T_F$. The QMD results are represented by the solid red circles. Comparing with the Lee–More model (κ_{LM}) widely used in hydrocodes, we find κ_{QMD} is higher by a factor of 3 to 10 in the warm regime ($T < T_F$). Such κ enhancement in the WDM regime has also been observed in previous publications.[59–64] To apply these FP-based κ_{QMD} to ICF simulations, we have fit the κ_{QMD} results by the following formula:[65]

$$\kappa_{QMD} = \frac{20\times(2/\pi)^{3/2} k_B^{7/2} T^{5/2}}{\sqrt{m_e}\, Z_{eff}\, e^4} \times \frac{0.095\times(Z_{eff}+0.24)}{1+0.24\, Z_{eff}} \times \frac{1}{(\ln\Lambda)_{QMD}} \qquad (18)$$

with the same Spitzer prefactor as used in κ_{LM} and Z_{eff} = 1 for deuterium. The generalized QMD Coulomb logarithm has the following form:

$$(\ln\Lambda)_{QMD} = \exp\left\{\alpha_0 + \sum_{i=1}^{5}\left[\alpha_i(\ln\Gamma)^i + \beta_i(\ln\theta)^i\right]\right\}. \qquad (19)$$

This fifth-order polynomial function of coupling and degeneracy parameters (Γ,θ) has been fit with the κ_{QMD} data using multivariable least-square fit. To allow κ_{QMD} to converge to κ_{LM} at the ideal plasma conditions ($\Gamma \ll 1$ and $\theta \gg 1$), we have added high-temperature points from κ_{LM} into the data set for the global fitting. The resulting fitting parameters are expressed in Table141.II. Overall, the global fit with the above parameters, depicted by Fig. 141.29, gives only a small error of ~5%. The

Table 141.II: The fitting parameters for the $(\ln \Lambda)_{QMD}$.

i	α_i	β_i
0	−0.740148	
1	−0.181459	+0.861554
2	$+6.396443 \times 10^{-4}$	−0.105704
3	$+1.479543 \times 10^{-3}$	-6.757829×10^{-3}
4	-1.233616×10^{-4}	-1.69007×10^{-4}
5	-2.581072×10^{-5}	$+3.492008 \times 10^{-5}$

tabulated κ_{QMD} of deuterium can be found in the Supplementary Material of Ref. 65.

Finally, we examine the QMD-predicted opacities by comparing them to the cold-opacity-patched AOT in Figs. 141.30 and 141.31 for the deuterium density ρ_D = 7.391 g/cm^3. It is noted that the cold-opacity–patched AOT is currently used in our hydrocodes for radiation-transport simulations with the multigroup diffusion scheme. The total Rosseland opacity is plotted in Fig. 141.30 as a function of the plasma temperature. As the plasma temperature approaches T_F, the QMD opacity at T = 43.09 eV converges to the AOT value. Below ~30 eV, no data exist in the AOT for the warm dense regime. Historically, the cold opacity of solid deuterium had been patched into the AOT for ICF hydro simulations. Figure 141.30 illustrates that the QMD opacities in the WDM conditions are much higher than the cold opacities. Namely, the density-scaled cold opacities significantly underestimated the photon absorption of warm dense plasmas. This is understandable because as deuterium is compressed to this density (>35× compression) from solid D_2 and warms up to above ~10,000 K, energy gaps are filled and the density of states increases in such systems. As a result, photon absorptions become more probable than the cold solid case, leading to higher opacities. Figures 141.31(a) and 141.31(b) plot the corresponding grouped opacities as a function of the central photon energy in each group for plasma temperatures of T = 10.77 eV and T = 43.09 eV, respectively (48 photon-energy groups were used). Figure 141.31(a) shows that at the low plasma temperature of T = 10.77 eV, the grouped opaci-

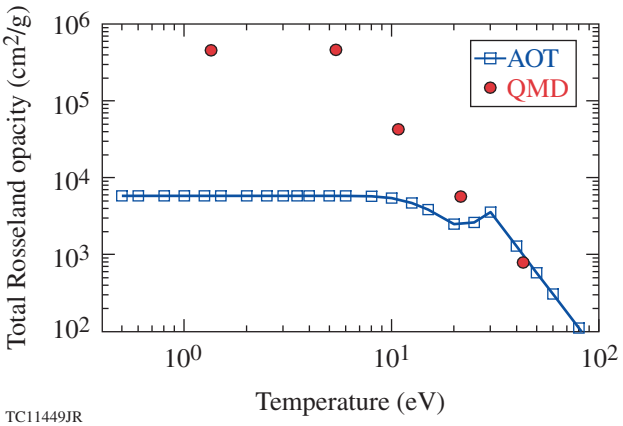

Figure 141.30
The total Rosseland opacity of deuterium as a function of the plasma temperature at a density of $\rho_D \simeq 7.391$ g/cm^3, which are compared between the cold-opacity–patched AOT and the QMD calculations.

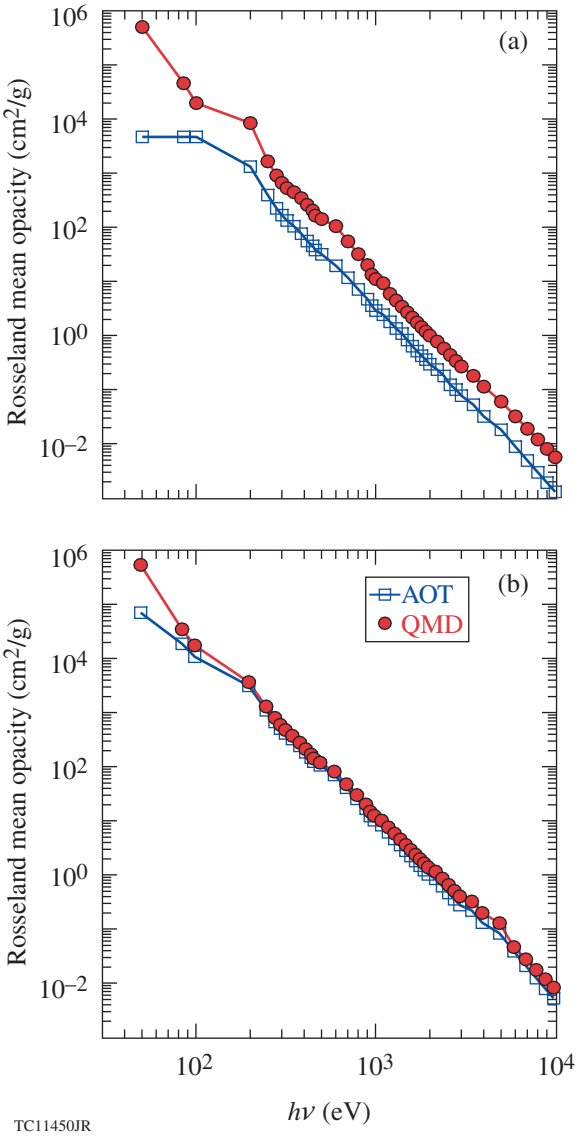

Figure 141.31
The grouped Rosseland mean opacity as a function of the photon energy $h\nu$, for the deuterium density of $\rho_D \simeq 7.391$ g/cm^3 at temperatures of (a) $T \simeq 10.77$ eV and (b) $T \simeq 43.09$ eV.

ties from QMD calculations become overall higher than the cold-opacity values. For photon-energy groups of $h\nu < 2$ keV (important to ICF), the QMD opacity is enhanced by a factor of 3 to 100, depending on $h\nu$. When the plasma temperature increases to $T = 43.09$ eV, Fig. 141.31(b) indicates that both the QMD and AOT opacities begin to agree with each other over a wide range of photon energies, except for the first two groups at $h\nu = 50$ eV and $h\nu = 85$ eV.

The first-principles opacity tables (FPOT) of deuterium and DT have been built from these QMD calculations for a wide range of densities ($\rho_D = 0.5$ to 673.518 g/cm^3) and temperatures (from $T = 5000$ K up to the Fermi temperature for each density point). For higher temperature points ($T > T_F$), we have incorporated the AOT data into the FPOT table since the FP calculations reproduced the AOT data at high-T plasma conditions, which are shown in Figs. 141.30 and 141.31. To make it compatible with our hydrocodes (*LILAC* and *DRACO*), we have created the FPOT in both the Rosseland and Planck mean opacities with 48 photon-energy groups for hydro simulations. The tabulated FPOT of deuterium can be found in the Supplementary Material of Ref. 76.

Impact of FP-Based Properties of DT on ICF Target Designs

With these FP-calculated tables of FPEOS, FPOT, and κ_{QMD} of DT (mass scaled from the deuterium properties) being implemented into our hydrocodes, we have investigated their combined effects on the 1-D prediction of ICF implosions through radiation–hydrodynamics simulations. The traditional physics models used in our 1-D hydrocode *LILAC*[107] were the *SESAME* for EOS, the Lee–More thermal conductivity (κ_{LM}), and the cold-opacity–patched AOT. We first examine a typical OMEGA implosion in Figs. 141.32 and 141.33. The cryogenic DT target with a diameter of $\phi = 865$ μm [shown in Fig. 141.32(a)] consists of a thin (7.5-μm) double-layer plastic ablator and a 40-μm layer of DT ice. The 3.7-μm outer layer of Si-doped CH is used to reduce laser imprints.[108,109] The OMEGA target is driven by a triple-picket laser pulse[12,110,111] with a total energy of ~26 kJ, illustrated by Fig. 141.32(b). The peak laser intensity is ~10^{15} W/cm^2. The properly timed pickets set up a low-adiabat capsule for the main pulse to implode.

In Fig. 141.33 the hydro simulation results using the FP-based properties of DT (FPEOS/FPOT/κ_{QMD}) are compared with the traditional models of *SESAME*/AOT/κ_{LM}. The solid red lines represent the FP simulations, while the dashed blue lines

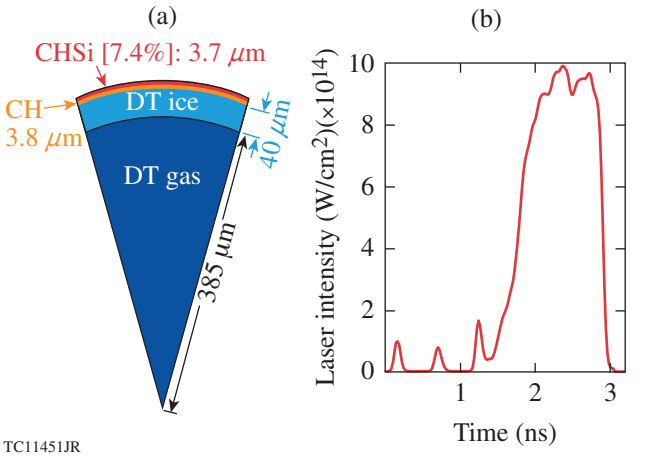

Figure 141.32
(a) A schematic diagram of cryogenic DT target on OMEGA; (b) the triple-picket pulse shape used for low-adiabat cryogenic DT implosions on OMEGA.

represent the "standard" model predictions. In Fig. 141.33(a), the density and electron temperature profiles of the imploding DT capsule, at the beginning of the deceleration phase ($t = 2.96$ ns), are plotted as a function of the target radius. We observe that the FP simulation gives a lower peak density of $\rho_D = 8.8$ g/cm^3 and a higher shell temperature of $T \simeq 38$ eV, in contrast to the standard model predictions of $\rho_D = 10.4$ g/cm^3 and $T \simeq 28$ eV, respectively. The major contributions to these changes come from EOS and opacity differences, while the thermal conductivity effect is relatively small at this stage. As previously discussed,[36,37,76] the stiffer behavior of DT in FPEOS at $P = 10$ to 100 Mbar causes part of the density drop; while the enhanced opacity from FPOT gives more radiation preheat in the warm dense DT shell, which increases the electron temperature and decreases the peak density inside the DT shell. Figure 141.33(b) displays the predicted minimum adiabat of the DT shell for the two simulations. It indicates that the FP-based simulation gives a higher adiabat of $\alpha \simeq 2.8$ in contrast to the model-predicted $\alpha \simeq 2$. These changes in plasma conditions of the DT shell can have a consequence in the overall target performance. Figure 141.33(c) illustrates the mass density and ion-temperature profiles at the peak compression ($t = 3.14$ ns). The peak density drops from $\rho = 354$ g/cm^3 in the *SESAME*/AOT/κ_{LM} model simulation to $\rho = 262$ g/cm^3 in the case of using FP-based DT properties (FPEOS/FPOT/κ_{QMD}). Also, the hot-spot pressure, ion temperature, and target convergence ratio are somewhat reduced in the FP simulation. These differences cause ~36% reduction in the 1-D neutron yield prediction for the FPEOS/FPOT/κ_{QMD} simulation, which is shown by Fig. 141.33(d). Finally, we compare the compression ρR history

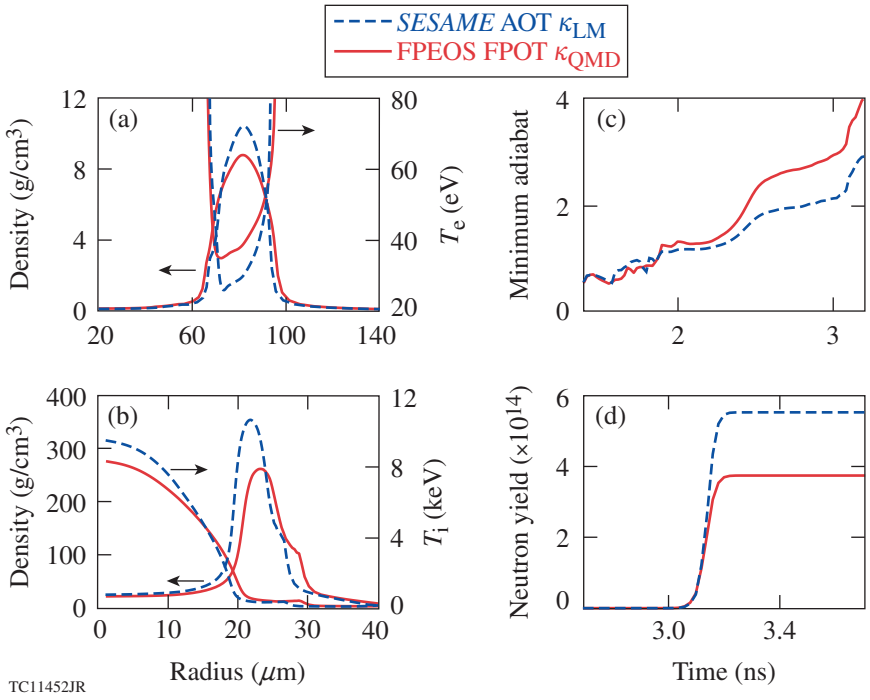

Figure 141.33
The hydro-simulation results using our first-principles–calculated properties of DT (solid red lines) are compared with the normal model simulation using *SESAME*-EOS, AOT, and the Lee–More thermal conductivity (dashed blue lines), for the OMEGA implosion shown in Fig. 141.32. The panels illustrate (a) the density and electron temperature profiles at t = 2.96 ns (the start of deceleration), (b) the minimum adiabat α as a function of time, (c) the density and ion temperature profile at peak compression (t = 3.14 ns), and (d) the neutron yield as a function of time.

in Fig. 141.34 for the two simulations. Consistent with the overall performance reduction, the FPEOS/FPOT/κ_{QMD} simulation gives a lower peak ρR than the model prediction. The neutron-averaged $\langle \rho R \rangle_n$ drops from 266 mg/cm^2 (*SESAME*-AOT-κ_{LM}) to 228 mg/cm^2 (FPOT/FPOT/κ_{QMD}). Namely, the compression ρR reduction is ~15% for this OMEGA implosion.

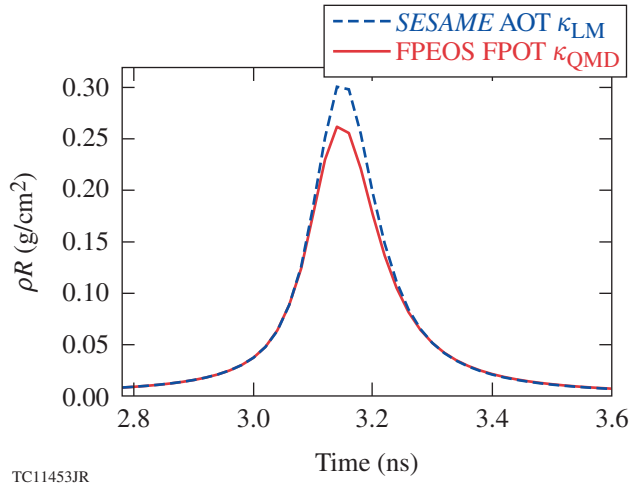

Figure 141.34
The predicted compression ρR's as a function of time are compared for the two simulations of the cryogenic DT implosion on OMEGA shown by Fig. 141.32. The neutron-averaged areal densities are $\langle \rho R \rangle_n$ = 266 mg/cm^2 (*SESAME*/AOT/κ_{LM}) and $\langle \rho R \rangle_n$ = 228 mg/cm^2 (FPOT/FPOT/κ_{QMD}), respectively.

Next, we study how the FP-based properties of DT affect the direct-drive–ignition target designs for the NIF. As a hydro-equivalent implosion to the OMEGA target discussed above, Fig. 141.35 shows the NIF target and the pulse shape, which are scaled from the hydro-equivalent OMEGA case shown in Fig. 141.32. The ϕ = 3452-μm target consists of a 36-μm CH/CHSi ablator layer and a 190-μm DT layer. The scaled laser pulse has a total energy of 1.5 MJ. According to the standard model prediction, this NIF ignition design should give a low-adiabat ($\alpha \simeq 2$) implosion. Again, we performed two 1-D hydro simulations using either the FP-based properties of DT or the standard plasma models. The simulation results are compared in Figs. 141.36 and 141.37. In Figs. 141.36(a) and 141.36(b), the density and temperature (T_e/T_i) profiles are plotted for the start of the deceleration stage (t = 13.0 ns) and the peak compression at t = 13.84 ns, respectively. Similar to what we have seen for the typical OMEGA implosion, the NIF results also show the reduced density and hot-spot ion temperature in the FPEOS/FPOT/κ_{QMD} simulation. The peak ion tem-

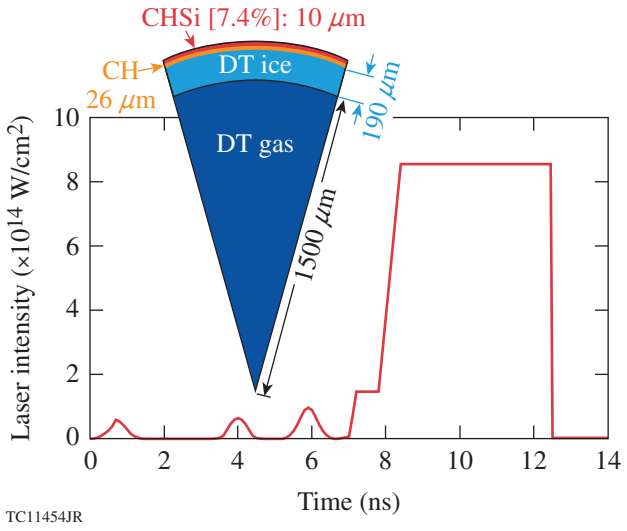

Figure 141.35
The model-predicted pulse shape for a direct-drive, low-adiabat ($\alpha \simeq 2$) ignition design for NIF, which is scaled from the OMEGA implosion shown in Fig. 141.32. The insert is a schematic diagram of a NIF target.

peratures inside the hot spot, illustrated by Fig. 141.36(b), are $T_i \simeq 10.9$ keV from the FP simulation, which is in contrast to the model-predicted $T_i \simeq 12.1$ keV. The peak density is also reduced to $\rho = 298$ g/cm^3 in the FPEOS/FPOT/κ_{QMD} simulation from the model-predicted $\rho = 371$ g/cm^3. These variations in ion temperature and peak compression can further affect the ignition burn-wave propagation. Figure 141.37(a) compares the FPEOS/FPOT/κ_{QMD} and SESAME/AOT/κ_{LM} simulations, at the start of burn-wave propagation (t = 13.86 ns). Now, the burn-wave–generated high pressure "reshocks" the shell and the resulting peak-density has a larger discrepancy: ρ = 532 g/cm^3 [*SESAME*/AOT/κ_{LM}] versus ρ = 366 g/cm^3 [FPEOS/FPOT/κ_{QMD}]; the temperature of burning plasmas in the hot spot varies from T_i = 17 keV to T_i = 13.4 keV, respectively. At the end, the total neutron yield changes from $Y = 2.1 \times 10^{19}$ [*SESAME*/AOT/κ_{LM}] to $Y = 1.2 \times 10^{19}$ [FPEOS/FPOT/κ_{QMD}], as indicated by Fig. 141.37(b). The energy gain varies accordingly by a factor of ~2, dropping from G = 40.0 to G = 23.4.

The degradation in target performance discussed above can be attributed to the plasma condition (ρ/T) changes in the in-flight DT shell. Namely, the model-predicted low adiabat ($\alpha \simeq 2$) is not reached in the imploding capsule. Instead, a higher adiabat is inferred from the FPEOS/FPOT/κ_{QMD} simulation. Therefore, to obtain a high-level gain (G = 40), we must use the FPEOS/FPOT/κ_{QMD} tables to retune the laser pulse so that the desired low-adiabat implosion can be recovered. As an

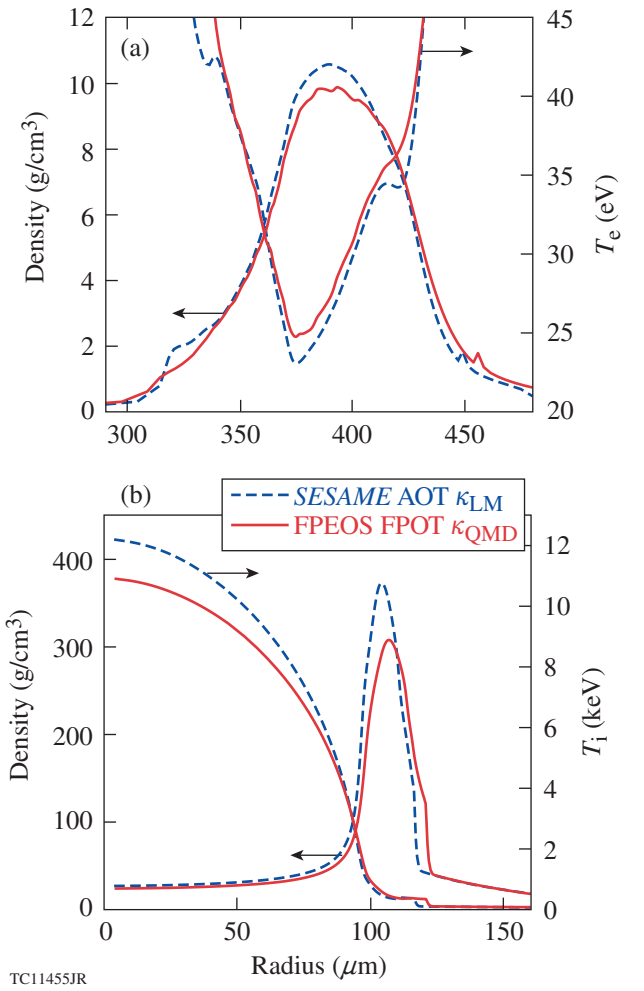

Figure 141.36
The hydro-simulation results using our first-principles–calculated properties of DT (solid red lines) are compared with the standard model simulation using *SESAME*-EOS, AOT, and the Lee–More thermal conductivity (dashed blue lines), for the NIF design shown in Fig. 141.35. The two panels indicate (a) the density and electron temperature profiles at t = 13.0 ns (the start of deceleration) and (b) the density and ion temperature as a function of radius at peak compression (t = 13.84 ns).

example, we show in Fig. 141.38(a) the fine-tuned pulse shape (solid red line) by using the FPEOS/FPOT/κ_{QMD} tables. The dashed blue line represents the original pulse shape predicted by the *SESAME*/AOT/κ_{LM} model. Compared to the original pulse, the retuned pulse has a slightly larger separation between the second and third pickets; also, the height of the main pulse's "step" is now both higher and longer than the original pulse. All these pulse changes place the target adiabat truly in the low level of $\alpha \simeq 2$, after the shock coalescence and enhanced radiation preheat are taken into account. Figure 141.38(b) indicates that the desired high-gain ($G \simeq 40$) implosion is now recovered with the retuned pulse using the FP-based properties of DT.

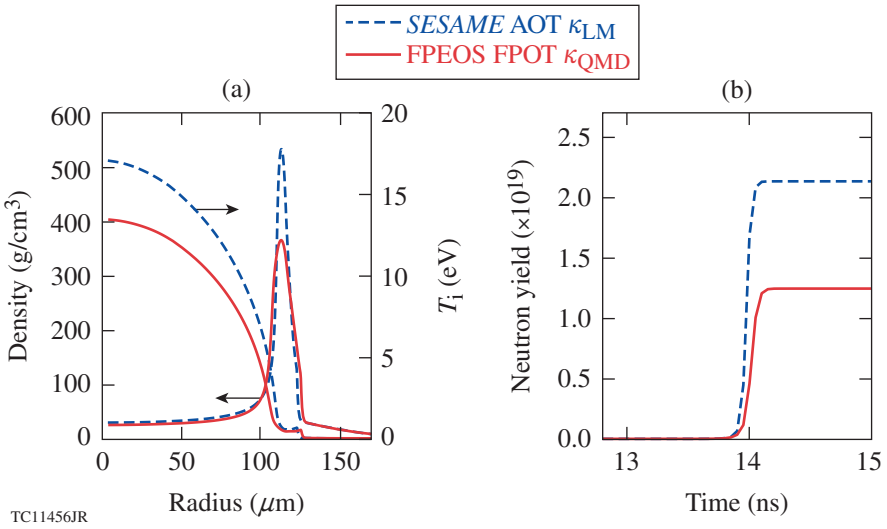

Figure 141.37
(a) Similar comparisons as shown in Fig. 141.36(b), but for a slightly later time (t = 13.86 ns) when the burn wave starts to propagate. The neutron production as a function of time is compared in (b) for the two simulations, in which the predicted energy gains are G = 40.0 (*SESAME*/AOT/κ_{LM}) and G = 23.4 (FPEOS/FPOT/κ_{QMD}), respectively.

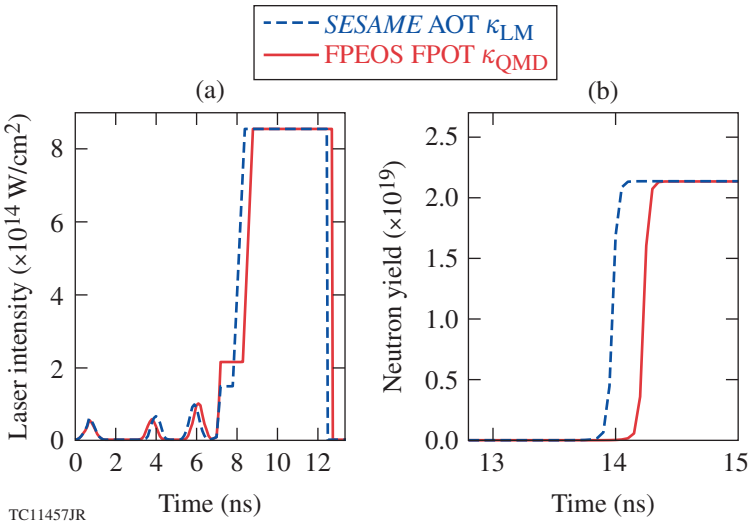

Figure 141.38
(a) The pulse shape (solid red line) was tuned by hydro-simulation using the first-principles properties of DT (FPEOS/FPOT/κ_{QMD}) to recover the high-gain level of $G \simeq 40$ for the same NIF target shown by the inset in Fig. 141.35. The dashed blue line indicates the original pulse shape predicted by the SESAME/AOT/κ_{LM} model for a similar gain level. The panel (b) shows the corresponding neutron yields predicted by hydro simulations using FPEOS/FPOT/κ_{QMD} and *SESAME*/AOT/κ_{LM}, for the same NIF target but different pulse shapes than illustrated in (a).

In Figs. 141.39 and 141.40, we further investigate a direct-drive NIF design with a very low adiabat ($\alpha \simeq 1.5$), which is the adiabat level often encountered in indirect-drive ICF implosions.[2–4] In such lower-adiabat implosions, the DT shells having higher ρ and lower T are in more strongly coupled and degenerate plasma conditions. Namely, the DT plasmas are readily in the WDM regime, and bigger differences between FPEOS/FPOT/κ_{QMD} and *SESAME*/AOT/κ_{LM} are expected. Here, the direct-drive NIF design uses a thin-layer (11-μm) HDC ablator. The HDC ablator has also been considered for indirect-drive target designs.[112] The thickness of DT ice is 180 μm with a target diameter of ϕ = 2982 μm. This relatively smaller target is intended to be driven by a low-intensity (~6 × 10^{14} W/cm^2), 1-MJ laser pulse (shown in Fig. 141.39). The implosion velocity is also relatively low: $v_{imp} \simeq 3 \times 10^7$ cm/s. The use of a mid-Z ablator and low-intensity pulse could avoid possible fast-electron preheat issues caused by the TPD instability.[113–116] The 1-D hydro-simulation results are presented in Fig. 141.40, where the peak density and T_i are compared for both FPEOS/FPOT/κ_{QMD} and *SESAME*/AOT/κ_{LM} simulations. Figure 141.40(a) shows the situation at the peak compression (t = 13.11 ns), while Fig. 141.40(b) illustrates the situation at the beginning of burn-wave propagation (t = 13.20 ns). Larger differences are seen in Fig. 141.40(b): ρ = 713 g/cm^3 versus ρ = 496 g/cm^3 and T_i = 20 keV versus T_i = 15.5 keV, respectively, from the *SESAME*/AOT/κ_{LM} and the FPEOS/FPOT/κ_{QMD} simulations. The final energy gain varies from the model-predicted G = 28.3 to G = 11.5 in the FP-based simulation. The variation is about a factor of ~2.5 between the two simulations, which is even larger than the α = 2 case discussed above.

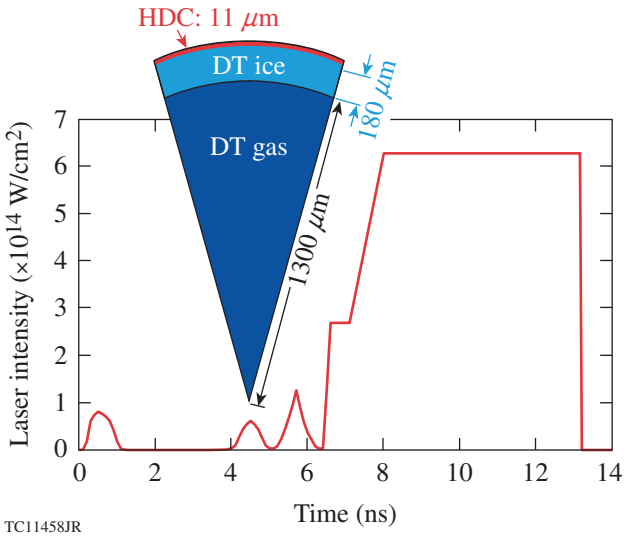

Figure 141.39
A very-low-adiabat ($\alpha \simeq 1.5$), low-implosion-velocity ($v_{imp} = 3.0 \times 10^7$ cm/s), direct-drive–ignition design for the NIF, which uses high-density carbon (HDC) as the thin-layer ablator. The target dimensions are illustrated in the inset. The mid-Z ablator and the lower peak intensity (~6×10^{14} W/cm^2) can help to reduce the TPD instability to avoid possible fast-electron preheat.

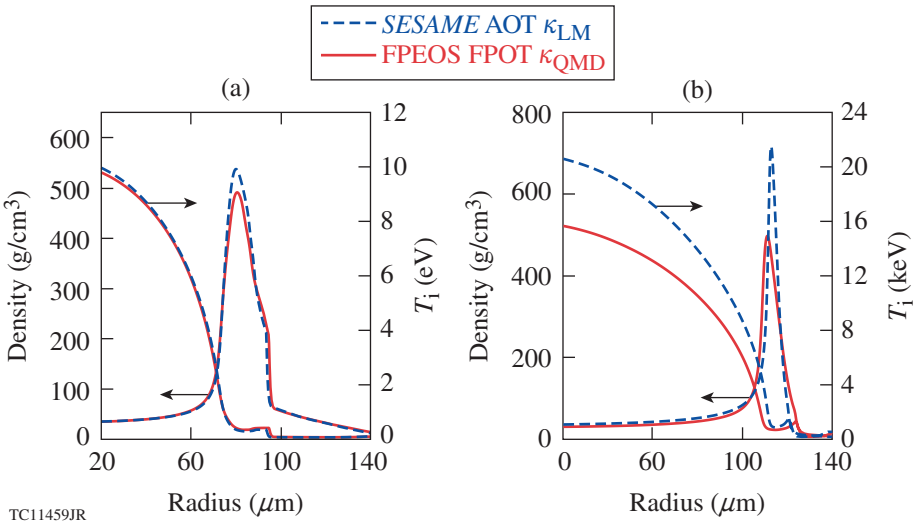

Figure 141.40
Simulation results for the thin HDC ablator target shown in Fig. 141.39: (a) the density and ion temperature profiles at the peak compression (t = 13.11 ns) and (b) the similar situation for a slightly later time (t = 13.20 ns) when the burn wave starts to propagate. The predicted energy gains are $G = 28.3$ (*SESAME*/AOT/κ_{LM}) and $G = 11.5$ (FPOT/FPOT/κ_{QMD}), respectively.

Summary

Combining the first-principles methods of PIMC and QMD, we have systematically derived accurate self-consistent properties of deuterium plasmas (or DT plasmas by mass scaling) over a wide range of densities and temperatures for ICF applications. They include the first-principles equation of state (FPEOS), the QMD-derived thermal conductivity (κ_{QMD}), and the first-principles opacity table (FPOT). Comparing these FP-based properties with the standard models adopted in hydrocodes, we found large discrepancies in the warm dense plasma regime. Implementing these FP-based tables into our hydrocodes, we have examined their combined effects on predicting ICF implosions, through hydro-simulations of both OMEGA targets and NIF ignition target designs. In predicting target performance between the FPEOS/FPOT/κ_{QMD} simulation and the usual models *SESAME*/AOT/κ_{LM}, changes of up to a factor of ~2.5 have been seen. The differences are caused by the adiabat increase, related to the stiffer behavior of DT in the pressure range of P = 10 to 100 Mbar, the enhanced opacity of the warm dense DT shell, and the higher thermal conductivity in the shell. The lower the adiabat of an ICF imploding capsule, the more variations expected. The desired high-gain target, which is truly a low-adiabat implosion, should be designed with the FP-based properties of DT fuel.

The stopping power of α particles in warm dense DT plasmas, recently attracting much attention in model studies and classical-MD calculations,[117,118] remains to be investigated by first-principles methods. We also noted that the ablator materials (CH, CHSi, and C) were still simulated with the standard

models in the current study. Whether or not that might change the prediction of the overall target performance remains to be investigated in future studies. But if we follow the same spirit of systematic work on DT, we could extend such first-principles studies to ICF-relevant ablator materials in the near future. Completely knowing the warm-dense–plasma properties of both DT and ablator materials would not only be beneficial for reliable ICF target designs but also improve our understanding of material behavior under HED conditions in general. We also hope that such first-principles studies will facilitate future experiments in the relevant plasma conditions.

ACKNOWLEDGMENT

This material is based upon work supported by the Department of Energy National Nuclear Security Administration under Award Number DE-NA0001944, the University of Rochester, and the New York State Energy Research and Development Authority. The support of DOE does not constitute an endorsement by DOE of the views expressed in this article. This work was also supported by Scientific Campaign 10 at the Los Alamos National Laboratory, operated by Los Alamos National Security, LLC for the National Nuclear Security Administration of the U.S. Department of Energy under Contract No. DE-AC52-06NA25396. B. Militzer acknowledges support from NSF and NASA.

REFERENCES

1. J. Nuckolls *et al*., Nature **239**, 139 (1972).
2. S. W. Haan, J. D. Lindl, D. A. Callahan, D. S. Clark, J. D. Salmonson, B. A. Hammel, L. J. Atherton, R. C. Cook, M. J. Edwards, S. Glenzer, A. V. Hamza, S. P. Hatchett, M. C. Herrmann, D. E. Hinkel, D. D. Ho, H. Huang, O. S. Jones, J. Kline, G. Kyrala, O. L. Landen, B. J. MacGowan, M. M. Marinak, D. D. Meyerhofer, J. L. Milovich, K. A. Moreno, E. I. Moses, D. H. Munro, A. Nikroo, R. E. Olson, K. Peterson, S. M. Pollaine, J. E. Ralph, H. F. Robey, B. K. Spears, P. T. Springer, L. J. Suter, C. A. Thomas, R. P. Town, R. Vesey, S. V. Weber, H. L. Wilkens, and D. C Wilson, Phys. Plasmas **18**, 051001 (2011).
3. M. J. Edwards, J. D. Lindl, B. K. Spears, S. V. Weber, L. J. Atherton, D. L. Bleuel, D. K. Bradley, D. A. Callahan, C. J. Cerjan, D. Clark, G. W. Collins, J. E. Fair, R. J. Fortner, S. H. Glenzer, S. W. Haan, B. A. Hammel, A. V. Hamza, S. P. Hatchett, N. Izumi, B. Jacoby, O. S. Jones, J. A. Koch, B. J. Kozioziemski, O. L. Landen, R. Lerche, B. J. MacGowan, A. J. MacKinnon, E. R. Mapoles, M. M. Marinak, M. Moran, E. I. Moses, D. H. Munro, D. H. Schneider, S. M. Sepke, D. A. Shaughnessy, P. T. Springer, R. Tommasini, L. Bernstein, W. Stoeffl, R. Betti, T. R. Boehly, T. C. Sangster, V. Yu. Glebov, P. W. McKenty, S. P. Regan, D. H. Edgell, J. P. Knauer, C. Stoeckl, D. R. Harding, S. Batha, G. Grim, H. W. Herrmann, G. Kyrala, M. Wilke, D. C. Wilson, J. Frenje, R. Petrasso, K. Moreno, H. Huang, K. C. Chen, E. Giraldez, J. D. Kilkenny, M. Mauldin, N. Hein, M. Hoppe, A. Nikroo, and R. J. Leeper, Phys. Plasmas **18**, 051003 (2011).
4. C. Cherfils-Clérouin *et al*., J. Phys.: Conf. Ser. **244**, 022009 (2010).
5. D. D. Meyerhofer, R. L. McCrory, R. Betti, T. R. Boehly, D. T. Casey, T. J. B. Collins, R. S. Craxton, J. A. Delettrez, D. H. Edgell, R. Epstein, K. A. Fletcher, J. A. Frenje, V. Yu. Glebov, V. N. Goncharov, D. R. Harding, S. X. Hu, I. V. Igumenshchev, J. P. Knauer, C. K. Li, J. A. Marozas, F. J. Marshall, P. W. McKenty, P. M. Nilson, S. P. Padalino, R. D. Petrasso, P. B. Radha, S. P. Regan, T. C. Sangster, F. H. Séguin, W. Seka, R. W. Short, D. Shvarts, S. Skupsky, J. M. Soures, C. Stoeckl, W. Theobald, and B. Yaakobi, Nucl. Fusion **51**, 053010 (2011).
6. R. L. McCrory, R. Betti, T. R. Boehly, D. T. Casey, T. J. B. Collins, R. S. Craxton, J. A. Delettrez, D. H. Edgell, R. Epstein, J. A. Frenje, D. H. Froula, M. Gatu-Johnson, V. Yu. Glebov, V. N. Goncharov, D. R. Harding, M. Hohenberger, S. X. Hu, I. V. Igumenshchev, T. J. Kessler, J. P. Knauer, C. K. Li, J. A. Marozas, F. J. Marshall, P. W. McKenty, D. D. Meyerhofer, D. T. Michel, J. F. Myatt, P. M. Nilson, S. J. Padalino, R. D. Petrasso, P. B. Radha, S. P. Regan, T. C. Sangster, F. H. Séguin, W. Seka, R. W. Short, A. Shvydky, S. Skupsky, J. M. Soures, C. Stoeckl, W. Theobald, B. Yaakobi, and J. D. Zuegel, Nucl. Fusion **53**, 113021 (2013).
7. O. A. Hurricane *et al*., Nature **506**, 343 (2014).
8. S. X. Hu, V. N. Goncharov, and S. Skupsky, Phys. Plasmas **19**, 072703 (2012).
9. D. S. Clark *et al*., Phys. Plasmas **18**, 082701 (2011).
10. T. R. Dittrich *et al*., Phys. Rev. Lett. **112**, 055002 (2014).
11. S. X. Hu, P. B. Radha, J. A. Marozas, R. Betti, T. J. B. Collins, R. S. Craxton, J. A. Delettrez, D. H. Edgell, R. Epstein, V. N. Goncharov, I. V. Igumenshchev, F. J. Marshall, R. L. McCrory, D. D. Meyerhofer, S. P. Regan, T. C. Sangster, S. Skupsky, V. A. Smalyuk, Y. Elbaz, and D. Shvarts, Phys. Plasmas **16**, 112706 (2009).
12. S. X. Hu, V. N. Goncharov, P. B. Radha, J. A. Marozas, S. Skupsky, T. R. Boehly, T. C. Sangster, D. D. Meyerhofer, and R. L. McCrory, Phys. Plasmas **17**, 102706 (2010).
13. S. Atzeni and J. Meyer-ter-Vehn, *The Physics of Inertial Fusion: Beam Plasma Interaction, Hydrodynamics, Hot Dense Matter*, International Series of Monographs on Physics (Clarendon Press, Oxford, 2004).
14. S. X. Hu, V. A. Smalyuk, V. N. Goncharov, J. P. Knauer, P. B. Radha, I. V. Igumenshchev, J. A. Marozas, C. Stoeckl, B. Yaakobi, D. Shvarts, T. C. Sangster, P. W. McKenty, D. D. Meyerhofer, S. Skupsky, and R. L. McCrory, Phys. Rev. Lett. **100**, 185003 (2008).
15. R. C. Malone, R. L. McCrory, and R. L. Morse, Phys. Rev. Lett. **34**, 721 (1975).
16. V. N. Goncharov, T. C. Sangster, P. B. Radha, R. Betti, T. R. Boehly, T. J. B. Collins, R. S. Craxton, J. A. Delettrez, R. Epstein, V. Yu. Glebov, S. X. Hu, I. V. Igumenshchev, J. P. Knauer, S. J. Loucks, J. A. Marozas, F. J. Marshall, R. L. McCrory, P. W. McKenty, D. D. Meyerhofer, S. P. Regan, W. Seka, S. Skupsky, V. A. Smalyuk, J. M. Soures, C. Stoeckl, D. Shvarts, J. A. Frenje, R. D. Petrasso, C. K. Li, F. Séguin, W. Manheimer, and D. G. Colombant, Phys. Plasmas **15**, 056310 (2008).
17. S. X. Hu, V. Smalyuk, V. N. Goncharov, S. Skupsky, T. C. Sangster, D. D. Meyerhofer, and D. Shvarts, Phys. Rev. Lett. **101**, 055002 (2008).
18. S. Skupsky, Phys. Rev. A **16**, 727 (1977).
19. C. K. Li and R. D. Petrasso, Phys. Rev. Lett. **70**, 3059 (1993).

20. L. S. Brown, D. L. Preston, and R. L. Singleton, Jr., Phys. Rep. **410**, 237 (2005).
21. M. C. Herrmann, M. Tabak, and J. D. Lindl, Nucl. Fusion **41**, 99 (2001).
22. C. D. Zhou and R. Betti, Phys. Plasmas **15**, 102707 (2008).
23. R. Nora, R. Betti, K. S. Anderson, A. Shvydky, A. Bose, K. M. Woo, A. R. Christopherson, J. A. Marozas, T. J. B. Collins, P. B. Radha, S. X. Hu, R. Epstein, F. J. Marshall, R. L. McCrory, T. C. Sangster, and D. D. Meyerhofer, Phys. Plasmas **21**, 056316 (2014).
24. V. N. Goncharov, T. C. Sangster, R. Betti, T. R. Boehly, M. J. Bonino, T. J. B. Collins, R. S. Craxton, J. A. Delettrez, D. H. Edgell, R. Epstein, R. K. Follet, C. J. Forrest, D. H. Froula, V. Yu. Glebov, D. R. Harding, R. J. Henchen, S. X. Hu, I. V. Igumenshchev, R. Janezic, J. H. Kelly, T. J. Kessler, T. Z. Kosc, S. J. Loucks, J. A. Marozas, F. J. Marshall, A. V. Maximov, R. L. McCrory, P. W. McKenty, D. D. Meyerhofer, D. T. Michel, J. F. Myatt, R. Nora, P. B. Radha, S. P. Regan, W. Seka, W. T. Shmayda, R. W. Short, A. Shvydky, S. Skupsky, C. Stoeckl, B. Yaakobi, J. A. Frenje, M. Gatu-Johnson, R. D. Petrasso, and D. T. Casey, Phys. Plasmas **21**, 056315 (2014).
25. B. I. Bennett *et al*., Los Alamos National Laboratory, Los Alamos, NM, Report LA-7130 (1978).
26. G. I. Kerley, Sandia National Laboratory, Albuquerque, NM, Report SAND2003-3613 (2003).
27. G. I. Kerley, Phys. Earth Planet. Inter. **6**, 78 (1972).
28. Y. T. Lee and R. M. More, Phys. Fluids **27**, 1273 (1984).
29. B. Wilson *et al*., J. Quant. Spectrosc. Radiat. Transf. **99**, 658 (2006).
30. W. F. Huebner *et al*., Los Alamos National Laboratory, Los Alamos, NM, Report LA-6760-M (1977).
31. C. A. Iglesias and F. J. Rogers, Astrophys. J. **464**, 943 (1996).
32. C. Pierleoni *et al*., Phys. Rev. Lett. **73**, 2145 (1994).
33. B. Militzer and D. M. Ceperley, Phys. Rev. Lett. **85**, 1890 (2000).
34. B. Militzer *et al*., Phys. Rev. Lett. **87**, 275502 (2001).
35. V. S. Filinov *et al*., Plasma Phys. Control. Fusion **43**, 743 (2001).
36. S. X. Hu, B. Militzer, V. N. Goncharov, and S. Skupsky, Phys. Rev. Lett. **104**, 235003 (2010).
37. S. X. Hu, B. Militzer, V. N. Goncharov, and S. Skupsky, Phys. Rev. B **84**, 224109 (2011).
38. L. Collins *et al*., Phys. Rev. E **52**, 6202 (1995).
39. J. G. Clérouin and S. Bernard, Phys. Rev. E **56**, 3534 (1997).
40. J. Clérouin and J.-F. Dufrêche, Phys. Rev. E **64**, 066406 (2001).
41. L. A. Collins *et al*., Phys. Rev. B **63**, 184110 (2001).
42. M. P. Desjarlais, Phys. Rev. B **68**, 064204 (2003).
43. B. Holst, R. Redmer, and M. P. Desjarlais, Phys. Rev. B **77**, 184201 (2008).
44. L. Caillabet, S. Mazevet, and P. Loubeyre, Phys. Rev. B **83**, 094101 (2011).
45. L. A. Collins, J. D. Kress, and D. E. Hanson, Phys. Rev. B **85**, 233101 (2012).
46. M. A. Morales *et al*., High Energy Density Phys. **8**, 5 (2012).
47. J. Vorberger, D. O. Gericke, and W. D. Kraeft, High Energy Density Phys. **9**, 448 (2013).
48. C. Wang and P. Zhang, Phys. Plasmas **20**, 092703 (2013).
49. V. V. Karasiev *et al*., Phys. Rev. B **88**, 161108(R) (2013).
50. J. M. McMahon *et al*., Rev. Mod. Phys. **84**, 1607 (2012).
51. L. B. Da Silva *et al*., Phys. Rev. Lett. **78**, 483 (1997).
52. G. W. Collins *et al*., Science **281**, 1178 (1998).
53. A. N. Mostovych *et al*., Phys. Rev. Lett. **85**, 3870 (2000); A. N. Mostovych *et al*., Phys. Plasmas **8**, 2281 (2001).
54. M. D. Knudson *et al*., Phys. Rev. Lett. **87**, 225501 (2001).
55. M. D. Knudson *et al*., Phys. Rev. Lett. **90**, 035505 (2003).
56. V. E. Fortov *et al*., Phys. Rev. Lett. **99**, 185001 (2007).
57. D. G. Hicks, T. R. Boehly, P. M. Celliers, J. H. Eggert, S. J. Moon, D. D. Meyerhofer, and G. W. Collins, Phys. Rev. B **79**, 014112 (2009).
58. P. Loubeyre, S. Brygoo, J. Eggert, P. M. Celliers, D. K. Spaulding, J. R. Rygg, T. R. Boehly, G. W. Collins, and R. Jeanloz, Phys. Rev. B **86**, 144115 (2012).
59. V. Recoules *et al*., Phys. Rev. Lett. **102**, 075002 (2009).
60. F. Lambert *et al*., Phys. Plasmas **18**, 056306 (2011).
61. D. E. Hanson *et al*., Phys. Plasmas **18**, 082704 (2011).
62. B. Holst, M. French, and R. Redmer, Phys. Rev. B **83**, 235120 (2011).
63. C. E. Starrett *et al*., Phys. Plasmas **19**, 102709 (2012).
64. C. Wang *et al*., Phys. Rev. E **88**, 013106 (2013).
65. S. X. Hu, L. A. Collins, T. R. Boehly, J. D. Kress, V. N. Goncharov, and S. Skupsky, Phys. Rev. E **89**, 043105 (2014).
66. J. D. Kress *et al*., High Energy Density Phys. **7**, 155 (2011).
67. J. D. Kress *et al*., Phys. Rev. E **82**, 036404 (2010).
68. G. Faussurier *et al*., Phys. Plasmas **21**, 092706 (2014).
69. G. Dimonte and J. Daligault, Phys. Rev. Lett. **101**, 135001 (2008).
70. B. Jeon *et al*., Phys. Rev. E **78**, 036403 (2008).

71. J. N. Glosli *et al*., Phys. Rev. E **78**, 025401 (R) (2008).

72. L. X. Benedict *et al*., Phys. Rev. Lett. **102**, 205004 (2009).

73. B. Xu and S. X. Hu, Phys. Rev. E **84**, 016408 (2011).

74. L. X. Benedict *et al*., Phys. Rev. E **86**, 046406 (2012).

75. C. Blancard, J. Clérouin, and G. Faussurier, High Energy Density Phys. **9**, 247 (2013).

76. S. X. Hu, L. A. Collins, V. N. Goncharov, T. R. Boehly, R. Epstein, R. L. McCrory, and S. Skupsky, Phys. Rev. E **90**, 033111 (2014).

77. P. M. Celliers *et al*., Phys. Rev. Lett. **84**, 5564 (2000).

78. T. R. Boehly, D. H. Munro, P. M. Celliers, R. E. Olson, D. G. Hicks, V. N. Goncharov, G. W. Collins, H. F. Robey, S. X. Hu, J. A. Marozas, T. C. Sangster, O. L. Landen, and D. D. Meyerhofer, Phys. Plasmas **16**, 056302 (2009); T. R. Boehly, V. N. Goncharov, W. Seka, S. X. Hu, J. A. Marozas, D. D. Meyerhofer, P. M. Celliers, D. G. Hicks, M. A. Barrios, D. Fratanduono, and G. W. Collins, Phys. Plasmas **18**, 092706 (2011); T. R. Boehly, V. N. Goncharov, W. Seka, M. A. Barrios, P. M. Celliers, D. G. Hicks, G. W. Collins, S. X. Hu, J. A. Marozas, and D. D. Meyerhofer, Phys. Rev. Lett. **106**, 195005 (2011).

79. C. Wang, X.-T. He, and P. Zhang, Phys. Plasmas **18**, 082707 (2011).

80. S. Hamel, L. X. Benedict, P. M. Celliers, M. A. Barrios, T. R. Boehly, G. W. Collins, T. Döppner, J. H. Eggert, D. R. Farley, D. G. Hicks, J. L. Kline, A. Lazicki, S. LePape, A. J. Mackinnon, J. D. Moody, H. F. Robey, E. Schwegler, and P. A. Sterne, Phys. Rev. B **86**, 094113 (2012).

81. K. P. Driver and B. Militzer, Phys. Rev. Lett. **108**, 115502 (2012).

82. S. X. Hu, T. R. Boehly, and L. A. Collins, Phys. Rev. E **89**, 063104 (2014).

83. T. R. Mattsson *et al*., Phys. Rev. B **81**, 054103 (2010).

84. L. X. Benedict *et al*., Phys. Rev. B **89**, 224109 (2014).

85. R. F. Smith *et al*., Nature **511**, 330 (2014).

86. S. H. Glenzer *et al*., Science **327**, 1228 (2010).

87. A. L. Kritcher *et al*., Phys. Rev. Lett. **107**, 015002 (2011).

88. S. H. Glenzer *et al*., Phys. Rev. Lett. **90**, 175002 (2003).

89. S. P. Regan, K. Falk, G. Gregori, P. B. Radha, S. X. Hu, T. R. Boehly, B. J. B. Crowley, S. H. Glenzer, O. L. Landen, D. O. Gericke, T. Döppner, D. D. Meyerhofer, C. D. Murphy, T. C. Sangster, and J. Vorberger, Phys. Rev. Lett. **109**, 265003 (2012).

90. E. L. Pollock, Comput. Phys. Commun. **52**, 49 (1988).

91. D. M. Ceperley, Rev. Mod. Phys. **67**, 279 (1995).

92. D. M. Ceperley, in *Monte Carlo and Molecular Dynamics of Condensed Matter Systems*, edited by K. Binder and G. Ciccotti (Italian Physical Society, Bologna, Italy, 1996).

93. B. Militzer and E. L. Pollock, Phys. Rev. E **61**, 3470 (2000).

94. B. Militzer, Phys. Rev. Lett. **97**, 175501 (2006).

95. B. Militzer, Phys. Rev. B **79**, 155105 (2009).

96. P. Hohenberg and W. Kohn, Phys. Rev. **136**, B864 (1964).

97. W. Kohn and L. J. Sham, Phys. Rev. **140**, A1133 (1965).

98. N. D. Mermin, Phys. Rev. **137**, A1441 (1965).

99. G. Kresse and J. Hafner, Phys. Rev. B **47**, 558 (1993).

100. G. Kresse and J. Hafner, Phys. Rev. B **49**, 14,251 (1994).

101. J. P. Perdew, K. Burke, and M. Ernzerhof, Phys. Rev. Lett. **77**, 3865 (1996); *ibid*. **78**, 1396(E) (1997).

102. R. Kubo, J. Phys. Soc. Jpn. **12**, 570 (1957); D. A. Greenwood, Proc. Phys. Soc. Lond. **71**, 585 (1958).

103. F. Perrot, Laser Part. Beams **14**, 731 (1996).

104. For details of the *ABINIT* code, please refer to http://www.abinit.org/.

105. T. R. Boehly, D. G. Hicks, P. M. Celliers, T. J. B. Collins, R. Earley, J. H. Eggert, D. Jacobs-Perkins, S. J. Moon, E. Vianello, D. D. Meyerhofer, and G. W. Collins, Phys. Plasmas **11**, L49 (2004).

106. G. V. Boriskov *et al*., Phys. **48**, 553 (2003).

107. J. Delettrez, R. Epstein, M. C. Richardson, P. A. Jaanimagi, and B. L. Henke, Phys. Rev. A **36**, 3926 (1987).

108. S. X. Hu, G. Fiksel, V. N. Goncharov, S. Skupsky, D. D. Meyerhofer, and V. A. Smalyuk, Phys. Rev. Lett. **108**, 195003 (2012).

109. G. Fiksel, S. X. Hu, V. N. Goncharov, D. D. Meyerhofer, T. C. Sangster, V. A. Smalyuk, B. Yaakobi, M. J. Bonino, and R. Jungquist, Phys. Plasmas **19**, 062704 (2012).

110. V. N. Goncharov, T. C. Sangster, T. R. Boehly, S. X. Hu, I. V. Igumenshchev, F. J. Marshall, R. L. McCrory, D. D. Meyerhofer, P. B. Radha, W. Seka, S. Skupsky, C. Stoeckl, D. T. Casey, J. A. Frenje, and R. D. Petrasso, Phys. Rev. Lett. **104**, 165001 (2010).

111. T. C. Sangster, V. N. Goncharov, R. Betti, P. B. Radha, T. R. Boehly, D. T. Casey, T. J. B. Collins, R. S. Craxton, J. A. Delettrez, D. H. Edgell, R. Epstein, C. J. Forrest, J. A. Frenje, D. H. Froula, M. Gatu-Johnson, V. Yu. Glebov, D. R. Harding, M. Hohenberger, S. X. Hu, I. V. Igumenshchev, R. Janezic, J. H. Kelly, T. J. Kessler, C. Kingsley, T. Z. Kosc, J. P. Knauer, S. J. Loucks, J. A. Marozas, F. J. Marshall, A. V. Maximov, R. L. McCrory, P. W. McKenty, D. D. Meyerhofer, D. T. Michel, J. F. Myatt, R. D. Petrasso, S. P. Regan, W. Seka, W. T. Shmayda, R. W. Short, A. Shvydky, S. Skupsky, J. M. Soures, C. Stoeckl, W. Theobald, V. Versteeg, B. Yaakobi, and J. D. Zuegel, Phys. Plasmas **20**, 056317 (2013).

112. O. L. Landen, D. K. Bradley, D. G. Braun, V. A. Smalyuk, D. G. Hicks, P. M. Celliers, S. Prisbrey, R. Page, T. R. Boehly, S. W. Haan, D. H. Munro, R. G. Wallace, A. Nikroo, A. Hamza, J. Biener, C. Wild, E. Woerner, R. E. Olson, G. A. Rochau, M. Knudson, D. C. Wilson, H. F. Robey, G. W. Collins, D. Ho, J. Edwards, M. M. Marinak, B. A. Hammel, D. D. Meyerhofer, and B. J. MacGowan, J. Phys.: Conf. Ser. **112**, 022004 (2008).

113. D. H. Froula, B. Yaakobi, S. X. Hu, P.-Y. Chang, R. S. Craxton, D. H. Edgell, R. Follett, D. T. Michel, J. F. Myatt, W. Seka, R. W. Short, A. Solodov, and C. Stoeckl, Phys. Rev. Lett. **108**, 165003 (2012).

114. D. T. Michel, A. V. Maximov, R. W. Short, S. X. Hu, J. F. Myatt, W. Seka, A. A. Solodov, B. Yaakobi, and D. H. Froula, Phys. Rev. Lett. **109**, 155007 (2012).

115. S. X. Hu, D. T. Michel, D. H. Edgell, D. H. Froula, R. K. Follett, V. N. Goncharov, J. F. Myatt, S. Skupsky, and B. Yaakobi, Phys. Plasmas **20**, 032704 (2013).

116. J. F. Myatt, H. X. Vu, D. F. DuBois, D. A. Russell, J. Zhang, R. W. Short, and A. V. Maximov, Phys. Plasmas **20**, 052705 (2013).

117. L. S. Brown and R. L. Singleton, Phys. Rev. E **79**, 066407 (2009).

118. P. E. Grabowski *et al*., Phys. Rev. Lett. **111**, 215002 (2013).